

Runge-Kutta Central Discontinuous Galerkin BGK Method for the Navier-Stokes Equations

Tan Ren ¹, Jun Hu ², Tao Xiong³, Jing-Mei Qiu⁴

Abstract

In this paper, we propose a Runge-Kutta (RK) central discontinuous Galerkin (CDG) gas-kinetic BGK method for the Navier-Stokes equations. The proposed method is based on the CDG method defined on two sets of overlapping meshes to avoid discontinuous solutions at cell interfaces, as well as the gas-kinetic BGK model to evaluate fluxes for both convection and diffusion terms. Redundant representation of the numerical solution in the CDG method offers great convenience in the design of gas-kinetic BGK fluxes. Specifically, the evaluation of fluxes at cell interfaces of one set of computational mesh is right inside the cells of the staggered mesh, hence the corresponding particle distribution function for flux evaluation is much simpler than that in existing gas-kinetic BGK methods. As a central scheme, the proposed CDG-BGK has doubled the memory requirement as the corresponding DG scheme; on the other hand, for the convection part, the CFL time step constraint of the CDG method for numerical stability is relatively large compared with that for the DG method. Numerical boundary conditions have to be treated with special care. Numerical examples for 1D and 2D viscous flow simulations are presented to validate the accuracy and robustness of the proposed RK CDG-BGK method.

Keywords: Central discontinuous Galerkin method, gas-kinetic scheme, BGK model, Navier-Stokes equations, Computational fluid dynamics.

¹School of Aerospace Engineering, Beijing Institute of Technology, Beijing, 100081. E-mail: rentanx@gmail.com

²School of Aerospace Engineering, Beijing Institute of Technology, Beijing, 100081. E-mail: hu-jun@bit.edu.cn

³Department of Mathematics, University of Houston, Houston, 77004. E-mail: txiong@math.uh.edu.

⁴Department of Mathematics, University of Houston, Houston, 77004. E-mail: jingqiu@math.uh.edu.

1 Introduction

There are two scales in describing compressible flow motions: the kinetic scale via the Boltzmann equation describing the particle distribution function and the hydrodynamic scale via the Euler or Navier-Stokes equations describing macroscopic flow variables such as mass, momentum and energy. In a gas-kinetic representation, all flow variables are moments of particle distribution function; the Euler or Navier-Stokes equations can be derived from taking moments of the Boltzmann equation based on the Chapman-Enskog expansion [3]. In this paper, we are interested in numerically simulating Navier-Stokes equations via the Boltzmann scheme with high order accuracy.

In the past few decades, many computational efforts have been devoted to simulate Euler or Navier-Stokes equations in the field of computational fluid dynamics (CFD). Many of classical numerical methods for Navier-Stokes equations involve solving convection and viscous terms separately on one set of computational grid. For the nonlinear convection term, the design of numerical fluxes at element interfaces is crucial to the success of numerical algorithms. Various approximate Riemann solvers have been proposed to approximate the wave structure of exact Riemann solutions, e.g. Godunov scheme [9], the approximate Riemann solvers due to Roe [30], Osher [29], Harten, Lax and van Leer [11], etc. For a summary on this topic, see [33]. For the viscous diffusion term, central difference method is often used. Another approach is to design fluxes at cell interfaces based on integrating particle distribution function in the phase space at kinetic scale. The kinetic flux vector splitting method for the Euler equations (KFVS-Euler) based on the collisionless Boltzmann equation is introduced in [25]. When viscous effect is considered, the particle distribution function contains both equilibrium (Maxwellian) and nonequilibrium parts of the gas flow; the inviscid and viscous terms can be treated simultaneously. For example, the kinetic flux vector splitting method for Navier-Stokes equations (KFVS-NS) was developed by introducing the nonequilibrium term in particle distribution obtained by Chapman-Enskog expansion in [4]; the gas-kinetic BGK method for Navier-Stokes equations (BGK-NS) was introduced in [40, 36].

To improve the performance of numerical schemes, high order schemes are introduced in 80's and underwent great development since then. For example, in the finite volume or finite difference framework, there are the second order MUSCL scheme [34], the essentially

non-oscillatory (ENO) scheme [10] and the weighted ENO (WENO) scheme [19, 12]. The discontinuous Galerkin (DG) method, as a class of finite element methods, has been very popular in the CFD community [7, 1, 8]. The high-order accuracy of DG is achieved by using high-order polynomial approximations within each element, where more than one degrees of freedom per element are stored and updated. The DG method has been well-known for its flexibility, h-p adaptivity, compactness and high parallel efficiency [5]. There have been many work in existing literatures in improving the BGK-NS method to be of high order accurate by interpolations or reconstructions such as WENO [24], by piecewise parabolic reconstruction of high order BGK fluxes [16], and by the DG framework [37, 18, 28]. These methods have been successfully applied in many engineering problems, such as the hypersonic viscous and heat conducting flows [15, 39, 17], 3D transonic flow [26], among many others. Comparisons between the schemes with approximate Riemann solvers and the particle distribution functions of the Boltzmann equation are provided in [24, 14].

The central scheme uses staggered meshes to avoid solving Riemann problems at cell interfaces and provides a black box solution to nonlinear hyperbolic conservation laws [27, 13]. Liu [20] introduced central schemes based on two sets of overlapping meshes. Taking advantages of the redundant representation of the solution on overlapping cells, approximate Riemann solvers are not needed at cell interfaces, and the high order total variation diminishing (TVD) Runge-Kutta (RK) methods can be directly applied by the method of lines approach. Following similar spirit, central DG (CDG) methods are proposed and developed for hyperbolic equations in [21], and central local DG methods are proposed for diffusion equations in [23].

We propose to couple the CDG framework [21] with the BGK-NS method [36] for Navier-Stokes simulations. Compared with the DG BGK methods [37, 18, 28], CDG methods evolve two pieces of approximate solutions defined on two sets of overlapping meshes. Such redundant representation of numerical solution offers great convenience in the design of gas-kinetic BGK fluxes. Specifically, the evaluation of fluxes at cell interfaces of one set of computational mesh is right inside a cell of the staggered mesh (i.e. continuous regions of the solution at the staggered mesh). Hence, the particle distribution function, without involving two different Maxwellian distributions from the left and right states and the corresponding

equilibrium state, is much simpler than existing gas-kinetic BGK methods [36, 37, 18, 28]. One of the key components that contributes to the success of the gas-kinetic BGK scheme [36] is the *exact time evolution of the BGK equation along characteristics*; such mechanism, despite its rather complicated formulation, brings the distribution function at cell interfaces to the equilibrium state in a very effective way. In the CDG framework, since the distribution function is continuous (at the interior of the other set of solution), such exact evolution is not as crucial. In our scheme, the method of lines approach is adopted; a third-order TVD RK method is used for temporal discretization. As the central scheme, the proposed CDG-BGK has doubled the memory requirement, since two sets of solutions have to be stored and updated simultaneously; on the other hand, for the convection part, the CFL time step constraint of the CDG method for numerical stability is relatively large compared with that for the DG method. The numerical boundary conditions have to be treated with special care. For example, a class of DG basis functions that preserves the given boundary condition, in the spirit of [6], are proposed for the wall boundary condition.

The paper is organized as follows. In Section 2, we propose the CDG-BGK method for one and two dimensional problems. The BGK fluxes, as well as numerical boundary conditions are discussed in details. In Section 3, following the pioneering work of [36], extensive numerical results are demonstrated to showcase the effectiveness of the proposed approach. We conclude the paper in Section 4.

2 CDG-BGK method for compressible Navier-Stokes equations

In this section, we first introduce a 1D BGK model and the corresponding macroscopic conservative Navier-Stokes equations in Section 2.1. We propose to use the central discontinuous Galerkin (CDG spatial discretization [20] coupled with a third-order total variation diminishing (TVD) Runge-Kutta (RK) temporal discretization [32] for solving the 1D BGK model in Section 2.2. The BGK type flux for both convection and viscous terms will be described in Section 2.3 and extension to multi-dimensional cases will be presented in Section 2.4. Finally we discuss the numerical boundary conditions in Section 2.5.

2.1 The 1D BGK model and Navier-Stokes equations

The integro-differential kinetic Boltzmann equation is commonly used to describe the evolution of the particle distribution function. To avoid the complicate bilinear collisional operator of the Boltzmann equation, a simplified BGK model was proposed by Bhatnagar et al. [2]. The BGK collisional operator is known to preserve the collisional invariant properties of mass, momentum and energy, as well as the entropy dissipation property.

For a 1D flow, the BGK model can be written as

$$f_t + uf_x = \frac{g - f}{\tau}, \quad (2.1)$$

where τ is the particle collision time, $f(t, x, u, \xi)$ is an unknown function of space variable x , time variable t , particle velocity u and internal variables ξ , $g(t, x, u, \xi)$ is the Maxwellian distribution given by

$$g = \rho \left(\frac{\lambda}{\pi} \right)^{\frac{K+1}{2}} e^{-\lambda[(u-U)^2 + \xi^2]}, \quad (2.2)$$

where ρ is the macroscopic density, λ is related to the gas temperature T by $\lambda = 1/(2RT)$, where R is the gas constant, U is the macroscopic velocity in the x direction, and $\xi^2 = \xi_1^2 + \xi_2^2 + \dots + \xi_K^2$. The total number of degrees of freedom in ξ is $K = (5 - 3\gamma)/(\gamma - 1) + 2$, where γ is the ratio of specific heats.

The relation between the macroscopic conservative variables and the microscopic distribution function f is

$$\mathbf{W} = (\rho, \rho U, E)^T = \int \boldsymbol{\psi} f \, d\Xi = \int \boldsymbol{\psi} g \, d\Xi, \quad (2.3)$$

where E is the total energy and

$$\boldsymbol{\psi} = (\psi_1, \psi_2, \psi_3)^T = \left(1, u, \frac{1}{2}(u^2 + \xi^2) \right)^T, \quad (2.4)$$

$d\Xi = dud\xi$ is the volume element in the phase space with $d\xi = d\xi_1 d\xi_2 \dots d\xi_K$.

The BGK collisional term is known to conserve the mass, momentum and energy. f and g satisfy the conservation constraint

$$\int \boldsymbol{\psi} \frac{g - f}{\tau} d\Xi = 0, \quad (2.5)$$

at any point in space and time. By taking moments of ψ to the BGK model (2.1), due to eq. (2.5), we get

$$\int \psi f_t d\Xi + \int u \psi f_x d\Xi = 0, \quad (2.6)$$

or

$$\mathbf{W}_t + \mathbf{G}_x = 0, \quad (2.7)$$

where \mathbf{W} is the vector of the macroscopic conservative variables in eq. (2.3). $\mathbf{G} = \int u \psi f d\Xi$ is the flux function from the kinetic formulation, specifically,

$$\mathbf{G} = \begin{pmatrix} G_\rho \\ G_m \\ G_E \end{pmatrix} = \int u \begin{pmatrix} 1 \\ u \\ \frac{1}{2}(u^2 + \xi^2) \end{pmatrix} f d\Xi, \quad (2.8)$$

where G_ρ is the density flux, G_m is the momentum flux, G_E is the energy flux.

The Chapman-Enskog expansion [3] gives $f = g - \tau(g_t + ug_x)$ up to the first order of τ , and from eq. (2.6), the compressible Navier-Stokes equations can be obtained [35]

$$\begin{pmatrix} \rho \\ \rho U \\ E \end{pmatrix}_t + \begin{pmatrix} \rho U \\ \rho U^2 + p \\ U(E + p) \end{pmatrix}_x = \begin{pmatrix} 0 \\ s_{1x} \\ s_{2x} \end{pmatrix}_x, \quad (2.9)$$

where $s_{1x} = \mu[\frac{2K}{K+1}U_x]$, $s_{2x} = \mu[\frac{K+3}{4}T_x + \frac{2K}{K+1}UU_x]$ are the viscous terms, $\mu = \tau p$ is the dynamic viscosity coefficient, the energy density is given by $E = \frac{1}{2}\rho(U^2 + \frac{K+1}{2\lambda})$ and $p = \rho/(2\lambda)$ is the pressure (see the Appendix A.1 for detailed description of these physical variables). For a monatomic gas, $\gamma = 5/3$, $K = 2$, the above Navier-Stokes equations become,

$$\begin{pmatrix} \rho \\ \rho U \\ E \end{pmatrix}_t + \begin{pmatrix} \rho U \\ \rho U^2 + p \\ U(E + p) \end{pmatrix}_x = \begin{pmatrix} 0 \\ \frac{4}{3}\mu U_x \\ \frac{5}{4}\mu T_x + \frac{4}{3}\mu UU_x \end{pmatrix}_x. \quad (2.10)$$

2.2 The RK CDG method

We propose to use the RK CDG method [21] to solve eq. (2.7). The CDG method evolves two sets of approximate solutions defined on overlapping meshes. Compared with the DG

method, the CDG method does not need a numerical flux to define the interface values. The evaluation of the flux at the interface of one mesh is right inside a cell of the other staggered mesh. The CDG method uses the flux function of the solution at the staggered mesh, which has no ambiguous values there. This is convenient for us to define the BGK flux in the next subsection. In the following, we first follow [21] to describe the CDG method.

Consider a 1D domain $[0, L]$ with a partition of $\{x_i\}_{i=1}^{i=N}$. Denote $x_{i+\frac{1}{2}} = \frac{1}{2}(x_i + x_{i+1})$, and let $I_i = [x_{i-\frac{1}{2}}, x_{i+\frac{1}{2}}]$ and $I_{i+\frac{1}{2}} = [x_i, x_{i+1}]$ be two sets of overlapping meshes. Two discrete spaces associated with the overlapping meshes I_i and $I_{i+\frac{1}{2}}$ are defined as

$$\begin{aligned}\mathbf{Z}_h &= \mathbf{Z}_h^k = \{\mathbf{z} : \text{each of its components } z|_{I_i} \in P^k(I_i), \forall i\}, \\ \mathbf{W}_h &= \mathbf{W}_h^k = \{\mathbf{z} : \text{each of its components } z|_{I_{i+\frac{1}{2}}} \in P^k(I_{i+\frac{1}{2}}), \forall i\},\end{aligned}$$

where the local space $P^k(I)$ consists of polynomials of degree at most k on I .

The semi-discrete CDG method for solving (2.7) is given as follows: find two sets of approximate solutions $\mathbf{W}_h^Z \in \mathbf{Z}_h$ and $\mathbf{W}_h^W \in \mathbf{W}_h$, such that for any $\boldsymbol{\eta}_h \in \mathbf{Z}_h$, $\boldsymbol{\zeta}_h \in \mathbf{W}_h$ and for all i ,

$$\begin{aligned}\frac{d}{dt} \int_{I_i} \mathbf{W}_h^Z \boldsymbol{\eta}_h \, dx &= \frac{1}{\Delta\tau^n} \int_{I_i} (\mathbf{W}_h^W - \mathbf{W}_h^Z) \boldsymbol{\eta}_h \, dx + \int_{I_i} \mathbf{G}(\mathbf{W}_h^W) \frac{d}{dx} \boldsymbol{\eta}_h \, dx \\ &\quad - \mathbf{G}(\mathbf{W}_h^W(x_{i+\frac{1}{2}}, t)) \boldsymbol{\eta}_h(x_{i+\frac{1}{2}}^-) + \mathbf{G}(\mathbf{W}_h^W(x_{i-\frac{1}{2}}, t)) \boldsymbol{\eta}_h(x_{i-\frac{1}{2}}^+),\end{aligned}\tag{2.11}$$

$$\begin{aligned}\frac{d}{dt} \int_{I_{i+\frac{1}{2}}} \mathbf{W}_h^W \boldsymbol{\zeta}_h \, dx &= \frac{1}{\Delta\tau^n} \int_{I_{i+\frac{1}{2}}} (\mathbf{W}_h^Z - \mathbf{W}_h^W) \boldsymbol{\zeta}_h \, dx + \int_{I_{i+\frac{1}{2}}} \mathbf{G}(\mathbf{W}_h^Z) \frac{d}{dx} \boldsymbol{\zeta}_h \, dx \\ &\quad - \mathbf{G}(\mathbf{W}_h^Z(x_{i+1}, t)) \boldsymbol{\zeta}_h(x_{i+1}^-) + \mathbf{G}(\mathbf{W}_h^Z(x_i, t)) \boldsymbol{\zeta}_h(x_i^+),\end{aligned}\tag{2.12}$$

where x_i^\pm are the right and left limits at the point x_i . Here the operations for vectors are component-wise operations. $\Delta\tau^n$ is the maximum time step determined by the CFL condition. The first terms on the right side of eqs. (2.11) and (2.12) are used to remove its $\mathcal{O}(1/\Delta t)$ dependency of numerical dissipation [21].

We focus our discussions on the approximate solution \mathbf{W}_h^Z on mesh I_i . It can be expressed as

$$\mathbf{W}_h^Z(x, t) = \sum_{l=0}^k \mathbf{W}_i^{Z,l}(t) \eta_i^l(x),\tag{2.13}$$

where $\{\eta_i^l\}$ is a basis function of $P^k(I_i)$. For example, the Legendre polynomials are a local orthogonal basis of $P^k(I_i)$. In the 1D case, $\eta_i^0 = 1$, $\eta_i^1 = (\frac{x-x_i}{\Delta x_i/2})$, $\eta_i^2 = (\frac{x-x_i}{\Delta x_i/2})^2 - \frac{1}{3}, \dots$,

where $\Delta x_i = x_{i+1/2} - x_{i-1/2}$. The approximate solution \mathbf{W}_h^W on mesh $I_{i+\frac{1}{2}}$ can be defined similarly. The integral in the first and second terms on the right side of eqs. (2.11)-(2.12) are numerically approximated by Gaussian quadrature rule. If the solutions are discontinuous, the TVB limiter proposed by Cockburn and Shu [7] will be used to eliminate spurious oscillations and enforce the stability.

The semi-discrete eqs. (2.11) and (2.12) are ordinary differential equations and can be written in a concise form $\frac{d}{dt}\mathbf{W} = L(\mathbf{W}, t)$, L is the spatial operator of the right side. In this paper, we use the third-order TVD RK time discretization [31] in the following form,

$$\begin{aligned}\mathbf{W}^{(1)} &= \mathbf{W}^n + \Delta t^n L(\mathbf{W}^n), \\ \mathbf{W}^{(2)} &= \frac{3}{4}\mathbf{W}^n + \frac{1}{4}\mathbf{W}^{(1)} + \frac{1}{4}\Delta t^n L(\mathbf{W}^{(1)}), \\ \mathbf{W}^{(n+1)} &= \frac{1}{3}\mathbf{W}^n + \frac{2}{3}\mathbf{W}^{(2)} + \frac{2}{3}\Delta t^n L(\mathbf{W}^{(2)}),\end{aligned}\tag{2.14}$$

where $\Delta t^n = \theta \Delta \tau^n$ is the current time step with $\theta \in (0, 1]$.

Remark 2.1. For the third-order TVD RK method (2.14), the CDG method has a little larger CFL number than the DG method for convection part, e.g., the CFL numbers of the CDG method are 0.58, 0.33, 0.22, while the CFL numbers of the DG method are 0.4, 0.2, 0.13, for P^1, P^2, P^3 respectively [22].

2.3 The BGK flux

In this section, we describe the BGK flux of the vector \mathbf{G} at cell interfaces for CDG method in eqs. (2.11)-(2.12), approximating the fluxes for the convection and viscous terms in Navier-Stokes equations (2.9). The BGK flux we described here mimics the Chapman-Enskog expansion [3].

Usually numerical solutions are discontinuous at cell interfaces and a numerical flux is needed to define the flux values at the cell interface. For example, based on the Euler limit, the KFVS-Euler method [25] splits the flux vector according to the particle velocity, and the distribution function is set to be

$$f_0 = \begin{cases} g^l, & \text{if } u \geq 0, \\ g^r, & \text{if } u \leq 0, \end{cases}$$

where g^l and g^r are the Maxwellian distributions at the left and right limits of the cell interface. Then based on the Navier-Stokes limit, the KFVS-NS method [4] uses the distribution function

$$f_0 = \begin{cases} g^l [1 + a^l x - \tau(a^l u + A^l)], & \text{if } x \leq 0, \\ g^r [1 + a^r x - \tau(a^r u + A^r)], & \text{if } x \geq 0, \end{cases} \quad (2.15)$$

where g^l and g^r are the same as the KFVS-Euler method, a^l, a^r are the spatial slopes and A^l, A^r are the temporal slopes from the left and right sides of the cell interface respectively. In [4], the spatial slopes are obtained by a MUSCL reconstruction. The exact solution of the distribution function, ignoring the BGK collisional term, is $f = f_0(x - ut)$.

Later, a gas-kinetic BGK method [36] obtains the distribution function at cell interfaces by integrating eq. (2.1) along the characteristics,

$$f(x_{j+\frac{1}{2}}, t, u, v, \xi) = \frac{1}{\tau} \int_0^t g(x', t', u, v, \xi) e^{-(t-t')/\tau} dt' + e^{-t/\tau} f_0(x_{j+\frac{1}{2}} - ut), \quad (2.16)$$

where $x' = x_{j+\frac{1}{2}} - u(t - t')$ is the particle trajectory, f_0 is the initial distribution function and g is the equilibrium state. The initial distribution function f_0 is constructed in the same way as the KFVS-NS method in eq. (2.15). The equilibrium state

$$g = g_0 [1 + (1 - H[x])\bar{a}^l x + H[x]\bar{a}^r x + \bar{A}t], \quad (2.17)$$

where g_0 is the Maxwellian distribution function, \bar{a}^l, \bar{a}^r are the spatial slopes from the left and right sides of the cell interface, \bar{A} is the temporal slope, $H[x]$ is the Heaviside function defined as

$$H[x] = \begin{cases} 0, & \text{if } x \leq 0, \\ 1, & \text{if } x \geq 0. \end{cases}$$

We utilize the gas-kinetic BGK formulations (2.16)-(2.17) to define the flux for the CDG method. Since the cell interface on one set of mesh is right inside a cell of the staggered mesh, the solution at the staggered mesh is continuous for flux evaluation with

$$g^l = g^r = g_0, \quad a^l = a^r = \bar{a}^l = \bar{a}^r = a, \quad A^l = A^r = \bar{A} = A, \quad (2.18)$$

in eqs. (2.15) and (2.17). Due to eq. (2.18), if we integrate eq. (2.16) by using eqs. (2.15) and (2.17), a very simple form of the particle distribution function could be obtained

$$f = g_0 [1 - \tau(au + A) + tA]. \quad (2.19)$$

Note that one of the key components that contributes to the success of the gas-kinetic BGK scheme [36] is the *exact time evolution* of the BGK equation along characteristics; such mechanism brings the distribution function at cell interfaces to the equilibrium state in a very effective way. In the context of a CDG method, due to the fact that $g^l = g^r = g_0$ in equation (2.18), the exact time evolution is not as crucial. Instead of the tA term in equation (2.19) (first order in time approximation), we propose to use the third-order TVD RK method for time evolution, neglecting the term tA in equation (2.19). Thus, the particle distribution function becomes

$$f = g_0 [1 - \tau(au + A)]. \quad (2.20)$$

Similarly, the distribution function in KFVS-NS method with the condition (2.18) is

$$f = g_0 [1 - \tau(au + A) - aut].$$

By using the third-order TVD RK method for time evolution, we ignore the aut term, leading to a formulation the same as in eq. (2.20). In summary, under the CDG framework with the method of lines RK time discretization, the fluxes for the gas-kinetic BGK method and the KFVS-NS method coincide per RK stage.

In eq. (2.20), a is the spatial slope of the Maxwellian in x direction and it is in the form of

$$a = a_1 + a_2 u + \frac{1}{2} a_3 (u^2 + \xi^2). \quad (2.21)$$

It has a unique correspondence with the slopes of the macroscopic conservative variables,

$$\int a g_0 d\Xi = \frac{\partial \rho}{\partial x}, \quad \int a u g_0 d\Xi = \frac{\partial \rho U}{\partial x}, \quad \int a \frac{1}{2} (u^2 + \xi^2) g_0 d\Xi = \frac{\partial E}{\partial x}, \quad (2.22)$$

where the slopes of the macroscopic conservative variables can be obtained by directly taking derivatives of the DG polynomials. Eq. (2.22) can be rewritten in a matrix-vector form as

$$\Gamma(a_1, a_2, a_3)^T = \frac{1}{\rho} \left(\frac{\partial \rho}{\partial x}, \frac{\partial \rho U}{\partial x}, \frac{\partial E}{\partial x} \right)^T, \quad (2.23)$$

where

$$(\Gamma_{\alpha\beta}) = \left(\int g_0 \psi_\alpha \psi_\beta d\Xi / \rho \right) = \begin{pmatrix} 1 & U & \Phi_1 \\ U & U^2 + \frac{1}{2\lambda} & \Phi_2 \\ \Phi_1 & \Phi_2 & \Phi_3 \end{pmatrix}, \quad \alpha, \beta = 1, 2, 3, \quad (2.24)$$

with

$$\begin{aligned}\Phi_1 &= \frac{1}{2} \left(U^2 + \frac{K+1}{2\lambda} \right), & \Phi_2 &= \frac{1}{2} \left(U^3 + \frac{(K+3)U}{2\lambda} \right), \\ \Phi_3 &= \frac{1}{4} \left(U^4 + \frac{K^2 + 4K + 3}{4\lambda^2} + \frac{(2K+6)U^2}{2\lambda} \right).\end{aligned}$$

The matrix Γ is symmetric and can be efficiently inverted to determine the components of a in eq. (2.21). A is the temporal slope with the following form,

$$A = A_1 + A_2 u + \frac{1}{2} A_3 (u^2 + \xi^2),$$

where A_1, A_2, A_3 are uniquely determined by the compatibility condition

$$\int (au + A) \psi g_0 d\Xi = 0,$$

that is

$$\Gamma(A_1, A_2, A_3)^T = -\frac{1}{\rho} \int au \psi g_0 d\Xi, \quad (2.25)$$

where Γ is the same as eq. (2.24). After all parameters are determined, we can get the fluxes in eqs. (2.11) and (2.12) by taking the moments of $u\psi$ to the distribution function f given by eq. (2.20) (See Appendix A.2 for moments evaluation of the Maxwellian distribution function).

Remark 2.2. The second volume integral term on the right side of eq. (2.11) corresponds two parts of the solution \mathbf{W}_h^W , one is in the cell $I_{i-\frac{1}{2}}$ and the other is in the cell $I_{i+\frac{1}{2}}$. The flux function $\mathbf{G}(\mathbf{W}_h^W)$ in each part of the volume integral can be obtained from the same procedure as described above. Similar arguments hold for the second volume integral term on the right side of eq. (2.12).

Remark 2.3. For the Navier-Stokes equations, the viscous coefficient and pressure are related to the particle collision time τ . With a constant dynamical viscous coefficient μ , the collision time can be defined by $\tau = \mu/p$.

Remark 2.4. The BGK model corresponds to an unit Prandtl number Pr , we modify the energy flux by subtracting the heat flux and adding another one with a variable Prandtl number [36].

$$G_E^{new} = G_E + \left(\frac{1}{Pr} - 1 \right) q. \quad (2.26)$$

The heat flux q can be evaluated precisely,

$$q = \frac{1}{2} \int (u - U) ((u - U)^2 + \xi^2) f d\Xi = -\tau \int g (u - U) \left(\psi_3 - \psi_2 U + \frac{1}{2} U^2 \right) (au + A) d\Xi. \quad (2.27)$$

Remark 2.5. In eq. (2.22), the spatial derivative is directly taken on the approximate CDG polynomials. It would lead to a k^{th} order scheme with P^k polynomial space for viscous flow simulations. For convection dominated problems, the accuracy would still be $(k + 1)^{th}$ order. It would be verified by our numerical examples in Section 3.

2.4 Extension to multidimensional cases

In this subsection, we extend the proposed CDG-BGK method in previous subsections to multidimensional cases. The 2D BGK model can be written as

$$f_t + u f_x + v f_y = \frac{g - f}{\tau}. \quad (2.28)$$

The Maxwellian distribution g is

$$g = \rho \left(\frac{\lambda}{\pi} \right)^{\frac{K+2}{2}} e^{-\lambda[(u-U)^2 + (v-V)^2 + \xi^2]},$$

where u, v are the particle velocities and U, V are the macroscopic velocities, ρ, λ, ξ and K have the same meanings as the 1D case. By taking the moments of $\boldsymbol{\psi} = (\psi_1, \psi_2, \psi_3, \psi_4)^T = (1, u, v, \frac{1}{2}(u^2 + v^2 + \xi^2))^T$ to eq. (2.28), we can get the following system of macroscopic conservative equation

$$\int \boldsymbol{\psi} f_t d\Xi + \int u \boldsymbol{\psi} f_x d\Xi + \int v \boldsymbol{\psi} f_y d\Xi = 0, \quad (2.29)$$

or

$$\mathbf{W}_t + \mathbf{G}_x + \mathbf{H}_y = 0. \quad (2.30)$$

$\mathbf{W} = (\rho, \rho U, \rho V, E)^T$ is the vector of macroscopic conservative variables. $\mathbf{G} = \int u \boldsymbol{\psi} f d\Xi$ and $\mathbf{H} = \int v \boldsymbol{\psi} f d\Xi$ are flux functions. From eq. (2.29), a 2D compressible Navier-Stokes equations can be obtained [35],

$$\begin{pmatrix} \rho \\ \rho U \\ \rho V \\ E \end{pmatrix}_t + \begin{pmatrix} \rho U \\ \rho U^2 + p \\ \rho UV \\ U(E + p) \end{pmatrix}_x + \begin{pmatrix} \rho V \\ \rho UV \\ \rho V^2 + p \\ V(E + p) \end{pmatrix}_y = \begin{pmatrix} 0 \\ s_{1x} \\ s_{2x} \\ s_{3x} \end{pmatrix}_x + \begin{pmatrix} 0 \\ s_{1y} \\ s_{2y} \\ s_{3y} \end{pmatrix}_y, \quad (2.31)$$

where

$$\begin{aligned}
S_{1x} &= \mu \left[2U_x - \frac{2}{K+2}(U_x + V_y) \right], & S_{1y} &= \mu(U_y + V_x), \\
S_{2x} &= \mu(V_x + U_y), & S_{2y} &= \mu \left[2V_y - \frac{2}{K+2}(U_x + V_y) \right], \\
S_{3x} &= \mu \left[2UU_x + V(V_x + U_y) - \frac{2}{K+2}U(U_x + V_y) + \frac{K+4}{4}T_x \right], \\
S_{3y} &= \mu \left[U(U_y + V_x) + 2VV_y - \frac{2}{K+2}V(U_x + V_y) + \frac{K+4}{4}T_y \right],
\end{aligned}$$

and the total energy is $E = \frac{1}{2}\rho(U^2 + V^2 + \frac{K+2}{2\lambda})$.

We consider the following numerical discretization of a 2D rectangular domain $\Omega = [0, L_x] \times [0, L_y]$. Let $\{x_i\}_{i=1}^{i=N_x}$ and $\{y_j\}_{j=1}^{j=N_y}$ be partitions of $[0, L_x]$ and $[0, L_y]$ respectively, with $x_{i+\frac{1}{2}} = \frac{1}{2}(x_i + x_{i+1})$, $y_{j+\frac{1}{2}} = \frac{1}{2}(y_j + y_{j+1})$. Let $I_i = [x_{i-\frac{1}{2}}, x_{i+\frac{1}{2}}]$, $J_j = [y_{j-\frac{1}{2}}, y_{j+\frac{1}{2}}]$, $I_{i+\frac{1}{2}} = [x_i, x_{i+1}]$, $J_{j+\frac{1}{2}} = [y_j, y_{j+1}]$. Denote $\{D_{i,j}\}_{i,j}$ and $\{D_{i+\frac{1}{2},j+\frac{1}{2}}\}_{i,j}$ be two sets of overlapping meshes for Ω , with $D_{i,j} = I_i \times J_j$ and $D_{i+\frac{1}{2},j+\frac{1}{2}} = I_{i+\frac{1}{2}} \times J_{j+\frac{1}{2}}$, see Fig. 2.1. Two discrete spaces associated with the overlapping meshes $\{D_{i,j}\}_{i,j}$ and $\{D_{i+\frac{1}{2},j+\frac{1}{2}}\}_{i,j}$ are defined as

$$\begin{aligned}
\mathbf{Z}_h &= \mathbf{Z}_h^k = \{\mathbf{z} : \text{each of its components } z|_{D_{i,j}} \in P^k(D_{i,j}), \forall i, j\}, \\
\mathbf{W}_h &= \mathbf{W}_h^k = \{\mathbf{z} : \text{each of its components } z|_{D_{i+\frac{1}{2},j+\frac{1}{2}}} \in P^k(D_{i+\frac{1}{2},j+\frac{1}{2}}), \forall i, j\},
\end{aligned}$$

where the local space $P^k(D)$ consists of polynomials of degree at most k on D . Similar to the 1D case, the semi-discrete CDG scheme for solving eq. (2.30) is given as follows: find two sets of approximate solutions $\mathbf{W}_h^Z \in \mathbf{Z}_h$ and $\mathbf{W}_h^W \in \mathbf{W}_h$, such that for any $\boldsymbol{\eta}_h \in \mathbf{Z}_h$, $\boldsymbol{\zeta}_h \in \mathbf{W}_h$ and for all i and j ,

$$\begin{aligned}
\frac{d}{dt} \int_{D_{i,j}} \mathbf{W}_h^Z \boldsymbol{\eta}_h \, dx dy &= \frac{1}{\Delta \tau^n} \int_{D_{i,j}} (\mathbf{W}_h^W - \mathbf{W}_h^Z) \boldsymbol{\eta}_h \, dx dy + \int_{D_{i,j}} (\mathbf{G}(\mathbf{W}_h^W) \frac{d}{dx} \boldsymbol{\eta}_h + \mathbf{H}(\mathbf{W}_h^W) \frac{d}{dy} \boldsymbol{\eta}_h) \, dx dy \\
&\quad - \int_{y_{j-1/2}}^{y_{j+1/2}} (\mathbf{G}(\mathbf{W}_h^W(x_{i+\frac{1}{2}}, y, t)) \boldsymbol{\eta}_h(x_{i+\frac{1}{2}}^-, y) - \mathbf{G}(\mathbf{W}_h^W(x_{i-\frac{1}{2}}, y, t)) \boldsymbol{\eta}_h(x_{i-\frac{1}{2}}^+, y)) dy \\
&\quad - \int_{x_{i-1/2}}^{x_{i+1/2}} (\mathbf{H}(\mathbf{W}_h^W(x, y_{j+\frac{1}{2}}, t)) \boldsymbol{\eta}_h(x, y_{j+\frac{1}{2}}^-) - \mathbf{H}(\mathbf{W}_h^W(x, y_{j-\frac{1}{2}}, t)) \boldsymbol{\eta}_h(x, y_{j-\frac{1}{2}}^+)) dx,
\end{aligned} \tag{2.32}$$

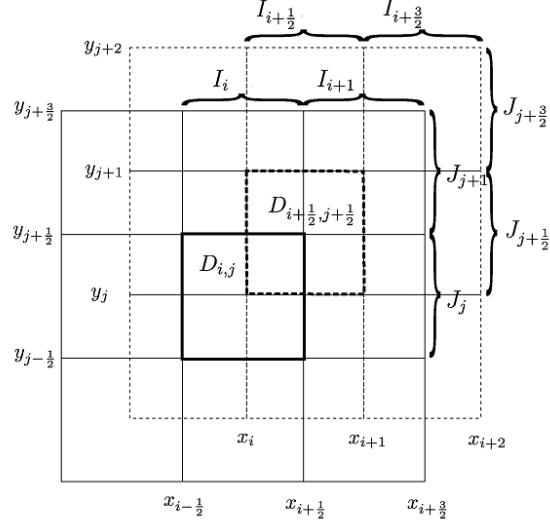


Figure 2.1: 2D overlapping meshes.

$$\begin{aligned}
\frac{d}{dt} \int_{D_{i+\frac{1}{2}, j+\frac{1}{2}}} \mathbf{W}_h^W \zeta_h \, dx dy &= \frac{1}{\Delta \tau^n} \int_{D_{i+\frac{1}{2}, j+\frac{1}{2}}} (\mathbf{W}_h^Z - \mathbf{W}_h^W) \zeta_h \, dx dy \\
&+ \int_{D_{i+\frac{1}{2}, j+\frac{1}{2}}} (\mathbf{G}(\mathbf{W}_h^Z) \frac{d}{dx} \zeta_h + \mathbf{H}(\mathbf{W}_h^Z) \frac{d}{dy} \zeta_h) \, dx dy \\
&- \int_{y_j}^{y_{j+1}} (\mathbf{G}(\mathbf{W}_h^Z(x_{i+1}, y, t)) \zeta_h(x_{i+1}^-, y) - \mathbf{G}(\mathbf{W}_h^Z(x_i, y, t)) \zeta_h(x_i^+, y)) \, dy \\
&- \int_{x_i}^{x_{i+1}} (\mathbf{H}(\mathbf{W}_h^Z(x, y_{j+1}, t)) \zeta_h(x, y_{j+1}^-) - \mathbf{H}(\mathbf{W}_h^Z(x, y_j, t)) \zeta_h(x, y_j^+)) \, dx.
\end{aligned} \tag{2.33}$$

Here the operations for vectors are component-wise operations. The approximate solution \mathbf{W}_h^Z on the element $D_{i,j}$ can be expressed as

$$\mathbf{W}_h^Z(x, y, t) = \sum_{l=0}^k \mathbf{W}_{i,j}^{Z,l}(t) \eta_{i,j}^l(x, y), \quad \text{for } x, y \in D_{i,j}. \tag{2.34}$$

The 2D Legendre polynomials $\eta_{i,j}^l$ are taken as a local orthogonal basis on $D_{i,j}$,

$$\begin{aligned}
\eta_{i,j}^0(x, y) &= 1, \quad \eta_{i,j}^1(x, y) = \frac{(x - x_i)}{\Delta x_i/2}, \quad \eta_{i,j}^2(x, y) = \frac{(y - y_j)}{\Delta y_j/2}, \\
\eta_{i,j}^3(x, y) &= \eta_{i,j}^1(x, y) \eta_{i,j}^2(x, y), \quad \eta_{i,j}^4(x, y) = (\eta_{i,j}^1(x, y))^2 - \frac{1}{3}, \quad \eta_{i,j}^5(x, y) = (\eta_{i,j}^2(x, y))^2 - \frac{1}{3},
\end{aligned}$$

where $\Delta x_i = x_{i+1/2} - x_{i-1/2}$, $\Delta y_j = y_{j+1/2} - y_{j-1/2}$. The approximate solution \mathbf{W}_h^W can be obtained similarly. The fluxes $\mathbf{G}(x, y, t)$ and $\mathbf{H}(x, y, t)$ at the cell interfaces and in the second

volume integral terms on the right side of eqs. (2.32) and (2.33) are calculated by the gas-kinetic formulation presented below. Please note that in 2D, the flux functions $\mathbf{G}(x, y, t)$ and $\mathbf{H}(x, y, t)$ in each of the volume integral terms corresponds to four parts of the solutions \mathbf{W}_h^W and \mathbf{W}_h^Z respectively, and the volume integrals are calculated by 2D Gaussian quadrature rules.

Similar to the 1D case, the distribution function f in eq. (2.28) can be expressed as

$$f = g_0 [1 - \tau(au + bv + A)], \quad (2.35)$$

up to the first order of τ . a, b are the spatial slopes in x and y directions respectively. They are in the form of

$$a = a_1 + a_2u + a_3v + \frac{1}{2}a_4(u^2 + v^2 + \xi^2), \quad b = b_1 + b_2u + b_3v + \frac{1}{2}b_4(u^2 + v^2 + \xi^2).$$

The components of a and b can be uniquely determined from the partial derivatives of the macroscopic conservative variables with respect to x, y ,

$$\begin{aligned} \int ag_0 d\Xi &= \frac{\partial \rho}{\partial x}, & \int bg_0 d\Xi &= \frac{\partial \rho}{\partial y}, \\ \int aug_0 d\Xi &= \frac{\partial \rho U}{\partial x}, & \int bvg_0 d\Xi &= \frac{\partial \rho U}{\partial y}, \\ \int avg_0 d\Xi &= \frac{\partial \rho V}{\partial x}, & \int bvg_0 d\Xi &= \frac{\partial \rho V}{\partial y}, \\ \int a\frac{1}{2}(u^2 + v^2 + \xi^2)g_0 d\Xi &= \frac{\partial E}{\partial x}, & \int b\frac{1}{2}(u^2 + v^2 + \xi^2)g_0 d\Xi &= \frac{\partial E}{\partial y}. \end{aligned} \quad (2.36)$$

The above equations can be written in a matrix-vector form as

$$\Gamma(a_1, a_2, a_3, a_4)^T = \frac{1}{\rho} \left(\frac{\partial \rho}{\partial x}, \frac{\partial \rho U}{\partial x}, \frac{\partial \rho V}{\partial x}, \frac{\partial E}{\partial x} \right)^T, \quad (2.37)$$

where

$$(\Gamma_{\alpha\beta}) = \left(\int g_0 \psi_\alpha \psi_\beta d\Xi / \rho \right) = \begin{pmatrix} 1 & U & V & \Phi_1 \\ U & U^2 + \frac{1}{2\lambda} & UV & \Phi_2 \\ V & UV & V^2 + \frac{1}{2\lambda} & \Phi_3 \\ \Phi_1 & \Phi_2 & \Phi_3 & \Phi_4 \end{pmatrix}, \quad (2.38)$$

with

$$\begin{aligned} \Phi_1 &= \frac{1}{2} \left(U^2 + V^2 + \frac{K+2}{2\lambda} \right), & \Phi_2 &= \frac{1}{2} \left(U^3 + UV^2 + \frac{(K+4)U}{2\lambda} \right), \\ \Phi_3 &= \frac{1}{2} \left(U^3 + U^2V + \frac{(K+4)V}{2\lambda} \right), & \Phi_4 &= \frac{1}{4} \left((U^2 + V^2)^2 + \frac{(K+4)(U^2 + V^2)}{\lambda} + \frac{K^2 + 6K + 8}{4\lambda^2} \right). \end{aligned}$$

Thus, a can be obtained by solving the linear system (2.37). Similar procedures can be used to get b . A is the temporal slope with the following form,

$$A = A_1 + A_2u + A_3v + \frac{1}{2}A_4(u^2 + v^2 + \xi^2),$$

where A_1, A_2, A_3, A_4 are uniquely determined by the compatibility condition

$$\int (au + bv + A)\boldsymbol{\psi}g_0 \, d\Xi = 0.$$

After a and b are determined, A_1, A_2, A_3, A_4 can be obtained by solving the following linear system

$$\Gamma(A_1, A_2, A_3, A_4)^T = -\frac{1}{\rho} \int (au + bv)\boldsymbol{\psi}g_0 \, d\Xi, \quad (2.39)$$

with Γ specified in eq. (2.38).

Finally the fluxes \mathbf{G} and \mathbf{H} in eqs. (2.32) and (2.33) can be obtained by taking the moments of $u\boldsymbol{\psi}$ and $v\boldsymbol{\psi}$ to the distribution function f of eq. (2.35) (see Appendix A.2 for moments evaluation of the 2D Maxwellian distribution function). The semi-discrete scheme of eqs. (2.32)-(2.33) will be evolved in time by the third-order TVD RK time method (2.14).

2.5 Numerical boundary conditions

For the numerical tests in this paper, we follow closely the examples in [36, 18], with similar boundary conditions, e.g. inflow, outflow and wall boundary conditions. In the CDG method, two sets of approximate solutions on overlapping meshes are updated; thus numerical boundary conditions are needed for both solutions. The inflow and outflow conditions can be treated, in a similar manner as those in DG, for both solutions in the CDG method. The more challenging case is the wall boundary conditions.

In the following, we take the Couette flow in a channel with the bottom wall fixed and the top wall moving (see Section 3.2) as an example to describe the proposed numerical no-slip boundary condition at both walls. Although the Couette flow is a 2D problem, it can be implemented as a 1D problem since the solutions do not depend on x . We assume the overlapping meshes in the y -direction as plotted in Fig. 2.2 with the walls located at y_0 and y_5 with $y_0 = 0, y_5 = 5$. Cells $J_0 = [y_{-\frac{1}{2}}, y_{\frac{1}{2}}]$ and $J_5 = [y_{\frac{9}{2}}, y_{\frac{11}{2}}]$ are cut through by the walls. For the no-slip boundary condition at wall, the physical macroscopic velocities

U, V are zero on the wall. However, the numerical ones might not be zero due to numerical errors; such non-zero errors might accumulated during long time evolution and eventually impact the effectiveness of the proposed scheme. We propose to enforce zero velocities at the numerical level. For example, on the bottom wall $y = 0$, we enforce $(\rho U)_{y_0} = (\rho V)_{y_0} = 0$, at the numerical level by the adopting a special set of basis functions. Specifically, in cell J_0 , we adopt the following basis functions

$$\eta_0^0 = 1, \quad \eta_0^1 = \left(\frac{y - y_0}{\Delta y_0/2} \right), \quad \eta_0^2 = \left(\frac{y - y_0}{\Delta y_0/2} \right)^2, \dots,$$

with

$$(\rho U)_h^Z = (\rho U)_0^0 \eta_0^0 + (\rho U)_0^1 \eta_0^1 + (\rho U)_0^2 \eta_0^2, \quad (\rho V)_h^Z = (\rho V)_0^0 \eta_0^0 + (\rho V)_0^1 \eta_0^1 + (\rho V)_0^2 \eta_0^2,$$

on J_0 , where $\Delta y_0 = y_{\frac{1}{2}} - y_{-\frac{1}{2}}$, and we enforce $(\rho U)_0^0 = (\rho V)_0^0 = 0$. In cell $J_{\frac{1}{2}}$, we adopt the basis functions

$$\zeta_{\frac{1}{2}}^0 = 1, \quad \zeta_{\frac{1}{2}}^1 = \left(\frac{y - y_{\frac{1}{2}}}{\Delta y_{\frac{1}{2}}/2} + 1 \right), \quad \zeta_{\frac{1}{2}}^2 = \left(\frac{y - y_{\frac{1}{2}}}{\Delta y_{\frac{1}{2}}/2} + 1 \right)^2, \dots,$$

with

$$(\rho U)_h^W = (\rho U)_{\frac{1}{2}}^0 \zeta_{\frac{1}{2}}^0 + (\rho U)_{\frac{1}{2}}^1 \zeta_{\frac{1}{2}}^1 + (\rho U)_{\frac{1}{2}}^2 \zeta_{\frac{1}{2}}^2, \quad (\rho V)_h^W = (\rho V)_{\frac{1}{2}}^0 \zeta_{\frac{1}{2}}^0 + (\rho V)_{\frac{1}{2}}^1 \zeta_{\frac{1}{2}}^1 + (\rho V)_{\frac{1}{2}}^2 \zeta_{\frac{1}{2}}^2,$$

on $J_{\frac{1}{2}}$ and $\Delta y_{\frac{1}{2}} = y_1 - y_0$, and enforce $(\rho U)_{\frac{1}{2}}^0 = (\rho V)_{\frac{1}{2}}^0 = 0$. The approximate solution in the ghost cell $J_{-\frac{1}{2}}$ is obtained in a mirror-symmetric manner with respect to the solution on cell $J_{\frac{1}{2}}$. Similar ideas of using a special set of basis to preserve the solution structure in DG methods can also be found in [6]. Boundary conditions can be set on the top wall $y = 5$ similarly.

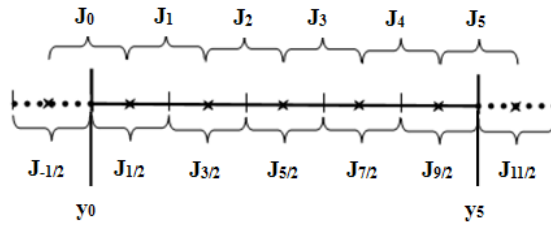


Figure 2.2: The 1D overlapping mesh for the Couette flow.

3 Numerical examples

In this section, we present simulation results of the proposed CDG-BGK method for several 1D and 2D viscous flow problems. For comparison, most of the examples are taken from [36, 18]. The maximum time step $\Delta\tau^n$ in eqs. (2.11), (2.12), (2.32) and (2.33) is chosen based on the CFL condition, while the time step in evolution is taken to be $\Delta t^n = 0.9\Delta\tau^n$ for all examples.

We define, in 1D cases,

$$\Delta\tau^n = \min\left(\frac{\text{CFL}_c h_x}{\text{Em}_x}, \frac{\text{CFL}_d h_x^2}{\mu}\right),$$

and in 2D cases,

$$\Delta\tau^n = \min\left(\text{CFL}_c / \left(\frac{\text{Em}_x}{h_x} + \frac{\text{Em}_y}{h_y}\right), \text{CFL}_d / \left(\frac{\mu}{h_x^2} + \frac{\mu}{h_y^2}\right)\right),$$

where $h_x = \min_i(\min(\Delta x_i, \Delta x_{i+\frac{1}{2}}))$ and $h_y = \min_j(\min(\Delta y_j, \Delta y_{j+\frac{1}{2}}))$, with $\Delta x_i = x_{i+1/2} - x_{i-1/2}$ and $\Delta x_{i+1/2} = x_{i+1} - x_i$, similarly for Δy_j and $\Delta y_{j+1/2}$. Em_x, Em_y are the maximum eigenvalues in x and y directions respectively. The eigenvalues are $U - c, U, U, U + c$ in the x direction and $V - c, V, V, V + c$ in the y direction for convection part, where $c = \sqrt{\gamma p / \rho}$ is the speed of sound. CFL_c and CFL_d are the CFL numbers for the convection and diffusion parts. In our numerical examples, for the third-order TVD Runge-Kutta method (2.14), we take $\text{CFL}_c = 0.58, 0.33, 0.22$ [22] and $\text{CFL}_d = 0.06, 0.01, 0.005$, for P^1, P^2 and P^3 solution spaces respectively. Our CFL_d numbers are larger than those taken in [23] for the central local DG method, yet they are working properly for all our numerical examples. The Prandtl number modification (2.26) will be used in all numerical examples except the laminar boundary layer case.

3.1 Accuracy test

We first solve the Navier-Stokes equations (2.7) with smooth solutions, where the initial conditions are given by

$$\rho(x, t = 0) = 1 + 0.2 \sin(\pi x), \quad U(x, t = 0) = 1, \quad p(x, t = 0) = 1. \quad (3.1)$$

The computational domain is $[0, 2]$ with periodic boundary condition. Two different viscosity coefficients are tested, $\mu = 0.00001$ and $\mu = 0.1$, corresponding to a convection-dominated

flow and a viscous flow, respectively. For this example, the Prandtl number is $Pr = 2/3$ and the ratio of specific heats is $\gamma = 5/3$. We compute the solutions up to time $t = 2$. TVB limiter is not used for this case. Since the exact solution is not available for this problem, the numerical errors and orders of density ρ are computed by comparing to the reference solution which is obtained by the P^3 solution space with 1280 cells. Here we take $\Delta\tau^n = \min\left(\frac{CFL_c h_x^{\frac{4}{3}}}{Em_x}, \frac{CFL_d h_x^2}{\mu}\right)$ for the P^3 case so that the temporal error is not dominated. The results are shown in Table 3.1. $(k+1)^{th}$ -order convergent rate can be observed for the proposed CDG-BGK scheme with $\mu = 0.00001$ and P^k solution spaces, while k^{th} -order convergent rate for even k and $(k+1)^{th}$ -order convergent rate for odd k can be observed for the solution with $\mu = 0.1$ and P^k solution spaces.

3.2 Couette flow

In the second example, we consider the couette flow in a channel of height H , with the bottom wall fixed and the top wall moving at a constant speed U_1 in the horizontal direction. The temperatures on the bottom and top walls are fixed with values $T_0 = 1/(2R\lambda_0)$ and $T_1 = 1/(2R\lambda_1)$ respectively. If the viscosity and heat conduction coefficients μ and κ_q are constant, an analytical solution for the steady state temperature distribution can be obtained, that is

$$\frac{T - T_0}{T_1 - T_0} = \frac{y}{H} + \frac{PrEc}{2} \frac{y}{H} \left(1 - \frac{y}{H}\right), \quad (3.2)$$

where the Eckert number is $Ec = U_1^2/(C_p(T_1 - T_0))$ and the definition of C_p can be found in Appendix A.1.

The solution of this problem does not depend on x , hence we solve it as a reduced 1D problem from eq. (2.30) in the y direction, that is,

$$\mathbf{W}_t + \mathbf{H}_y = 0,$$

i.e. the compressible Navier-Stokes equations (2.31) without the x -derivative term.

We take the computational domain to be $[0, 5]$ ($H = 5$) and divided by 5 cells with mesh size $\Delta y = 1$. The isothermal no-slip boundary condition is used on the bottom and top walls. Here we consider the temperature λ_0 and λ_1 at the boundaries with different ratios of specific heats $\gamma = 5/3, 7/5$, different Prandtl numbers $Pr = 0.72, 1.0$ and different Eckert

Table 3.1: Accuracy test, L^1 and L^∞ errors and orders for the initial condition (3.1) with P^1 , P^2 and P^3 solution spaces.

	N	L^1 error	order	L^∞ error	order
$\mu = 0.00001, P^1$	10	0.21E-02	–	0.34E-02	–
	20	0.78E-03	1.45	0.12E-02	1.50
	40	0.24E-03	1.72	0.36E-03	1.70
	80	0.65E-04	1.88	0.10E-03	1.86
	160	0.17E-04	1.94	0.26E-04	1.93
$\mu = 0.00001, P^2$	10	0.28E-03	–	0.46E-03	–
	20	0.36E-04	2.94	0.58E-04	2.98
	40	0.46E-05	2.98	0.73E-05	3.00
	80	0.58E-06	2.99	0.92E-06	3.00
	160	0.73E-07	2.99	0.12E-06	2.99
$\mu = 0.00001, P^3$	10	0.27E-04	–	0.38E-04	–
	20	0.16E-05	4.04	0.25E-05	3.95
	40	0.10E-06	4.02	0.15E-06	3.99
	80	0.63E-08	4.01	0.97E-08	3.99
	160	0.39E-09	4.00	0.61E-09	3.99
$\mu = 0.1, P^1$	10	0.10E-02	–	0.19E-02	–
	20	0.27E-03	1.93	0.52E-03	1.89
	40	0.68E-04	1.98	0.13E-03	1.97
	80	0.17E-04	2.00	0.33E-04	1.99
	160	0.42E-05	2.02	0.84E-05	2.00
$\mu = 0.1, P^2$	10	0.13E-03	–	0.22E-03	–
	20	0.35E-04	1.95	0.56E-04	1.94
	40	0.87E-05	1.99	0.14E-04	1.99
	80	0.22E-05	2.00	0.35E-05	2.00
	160	0.55E-06	2.00	0.89E-06	2.00
$\mu = 0.1, P^3$	10	0.93E-05	–	0.17E-04	–
	20	0.74E-06	3.65	0.14E-05	3.61
	40	0.49E-07	3.92	0.90E-07	3.93
	80	0.31E-08	3.99	0.56E-08	4.02
	160	0.19E-09	4.03	0.38E-09	3.89

Table 3.2: Boundary settings of λ_0 and λ_1 for Couette flow.

Pr	γ	Ec	λ_0	λ_1
0.72,1.0	5/3	10	1/1.19960	1/1.20040
0.72,1.0	5/3	50	1/1.19992	1/1.20008
0.72,1.0	7/5	10	1/1.42851	1/1.42863
0.72,1.0	7/5	50	1/1.42829	1/1.42886

numbers $Ec = 10, 50$. For specific settings, see Table 3.2. We take $U_1 = 0.1$ and $\mu = 0.1$. The initial conditions are

$$\rho(y, t = 0) = 1, \quad U(y, t = 0) = 0.1, \quad V(y, t = 0) = 0, \quad M(y, t = 0) = 0.1,$$

where $M = U/c$ is the Mach number.

The results with different boundary settings are shown in Figs. 3.1 and 3.2. The Prandtl number modification (2.26) is used in $Pr = 0.72$ cases. From the figures, we can see that: (1) numerical results match the analytical solutions very well with different parameters; (2) the implementation of the Prandtl number modification is needed compared with the analytical solutions and (3) P^2 solution space gives more accurate results than P^1 solution space with the same mesh size. Numerical error and order of convergence are summarized in Table 3.3. Roughly k^{th} order convergent rate is observed for the method with P^k polynomial space.

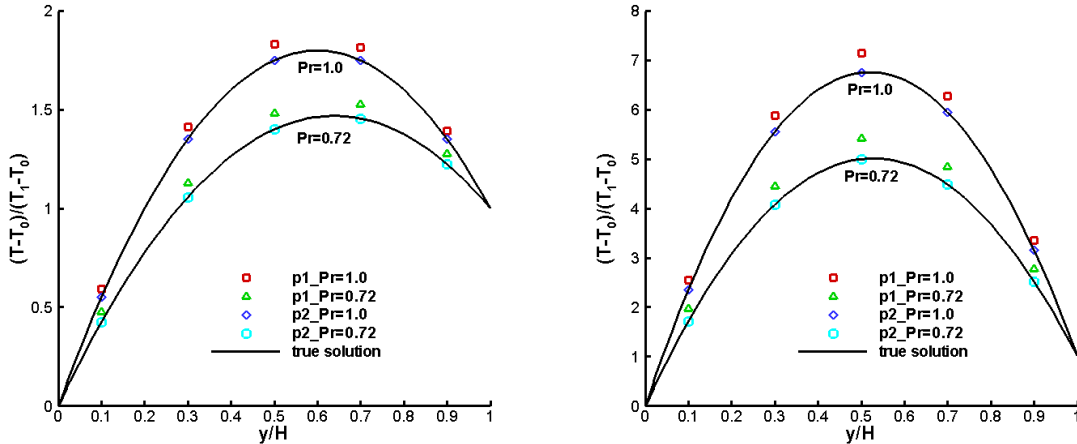


Figure 3.1: Temperature ratio $(T - T_0)/(T_1 - T_0)$ in the Couette flow with $\gamma = 5/3$. Left: $Ec = 10$. Right: $Ec = 50$.

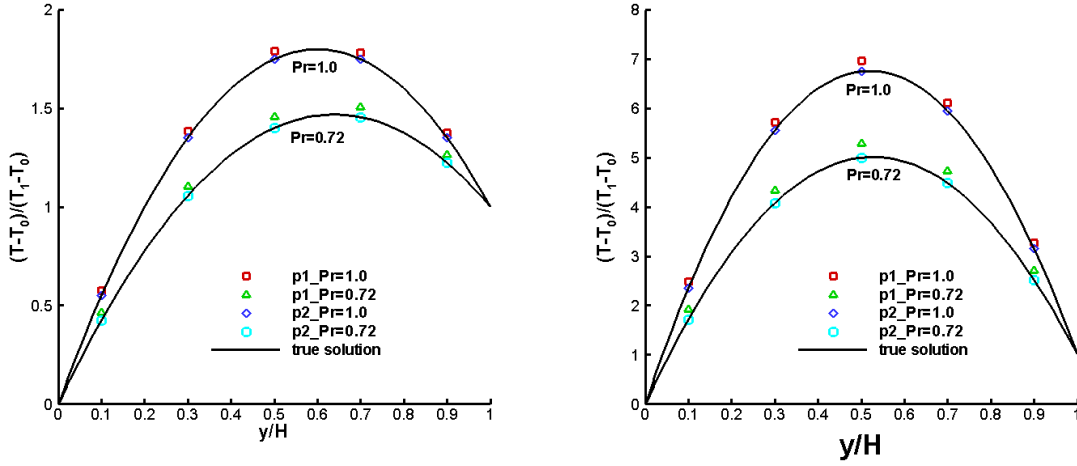


Figure 3.2: Temperature ratio $(T - T_0)/(T_1 - T_0)$ in the Couette flow with $\gamma = 7/5$. Left: $Ec = 10$. Right: $Ec = 50$.

Table 3.3: Couette flow, L^1 and L^∞ errors and orders for P^1 and P^2 solution spaces.

	N	L^1 error	order	L^∞ error	order
P^1	5	0.61E+00	–	0.66E+00	–
	10	0.19E+00	1.66	0.22E+00	1.60
	20	0.61E-01	1.65	0.74E-01	1.55
P^2	5	0.13E-03	–	0.16E-03	–
	10	0.30E-04	2.14	0.41E-04	1.96
	20	0.74E-05	2.04	0.11E-04	1.96
P^3	5	0.22E-04	–	0.28E-04	–
	10	0.35E-05	2.63	0.45E-05	2.62
	20	0.61E-06	2.51	0.82E-06	2.46

3.3 Navier-Stokes shock structure

Now we consider the shock structure problem for a monatomic gas by solving the Navier-Stokes equations (2.7). $\gamma = 5/3$ and the dynamical viscosity coefficient is $\mu = \mu_{-\infty}(T/T_{-\infty})^{0.8}$, $-\infty$ and ∞ denote the values at the upstream and downstream respectively. The dynamical viscosity coefficient at the upstream keeps to be a constant $\mu_{-\infty} = 0.0005$. The collision time τ in the BGK model is local via the relationship $\tau = \mu/p$ in each cell. The Mach number

$M = 1.5$ at the upstream and the Prandtl number $Pr = 2/3$. The initial conditions are

$$\begin{pmatrix} \rho \\ U \\ p \end{pmatrix}_{-\infty} = \begin{pmatrix} 1 \\ 1 \\ \frac{1}{\gamma M^2} \end{pmatrix}, \quad \begin{pmatrix} \rho \\ U \\ p \end{pmatrix}_{\infty} = \begin{pmatrix} \frac{(\gamma + 1)M^2}{2 + (\gamma - 1)M^2} \\ \frac{\gamma - 1}{\gamma + 1} + \frac{2}{(\gamma + 1)M^2} \\ \left(\frac{2\gamma}{\gamma + 1}M^2 - \frac{\gamma - 1}{\gamma + 1} \right) \frac{1}{\gamma M^2} \end{pmatrix}.$$

Symmetry boundary condition is used on the left and right boundaries. The reference solution can be obtained by integrating the steady state Navier-Stokes equations, with the corresponding Matlab programs available in Appendix C of [36].

The computational domain is $[-0.1, 0.1]$ and the mesh size $\Delta x = 1/800$ for both P^1 and P^2 cases. TVB limiter is used for this example. The results are presented in Fig. 3.3. In the figures, the normal stress and the heat flux are defined to be

$$\tau_{nn} = \frac{4}{3}\mu \frac{U_x}{2p}, \quad q_x = -\frac{5}{4} \frac{\mu}{Pr} \frac{T_x}{pc}.$$

From these results, we can see that the shock structure is captured well with a reasonable number of grid points. The difference between the results from P^1 and P^2 cases are very small.

3.4 Shock tube problem

In the fourth example, the Sod problem is tested by solving the Navier-Stokes equations (2.7) with $\gamma = 1.4$ and $Pr = 2/3$. The computational domain is $[-0.5, 0.5]$ with the mesh size $\Delta x = 1/200$. TVB limiter is used for this example. The initial conditions are

$$(\rho, U, p) = \begin{cases} (1, 0, 1), & x \leq 0, \\ (0.125, 0, 0.1), & x > 0. \end{cases} \quad (3.3)$$

Symmetry boundary condition is used on the left and right boundaries. We compute the solutions up to time $t = 0.2$. In Fig. 3.4, we show the results with a kinematic viscosity coefficient $\nu = \mu/\rho = 0.0005/(\rho\sqrt{\lambda})$. The solid lines are the reference solutions computed on a much refined mesh size $\Delta x = 1/1200$ with P^2 solution space. Both the shock and the contact discontinuity are captured well. From the zoom-in Fig. 3.5, we can see the P^2 case gives slightly better results than the P^1 case. The results with a smaller viscosity coefficient $\nu = \mu/\rho = 0.00005/(\rho\sqrt{\lambda})$ are presented in Fig. 3.6. The CDG-BGK method can capture the sharp discontinuity.

3.5 Laminar boundary layer

The last example is the 2D laminar boundary layer problem over a flat plate and we solve the 2D Navier-Stokes equations (2.30). The wall starts from $x = 0$ with a length of $L = 3$ at $y = 0$. A uniform rectangular mesh with 480×120 cells is used on the computational domain $[-1, 3] \times [0, 1]$. The initial conditions are set to be

$$\rho(x, y, t = 0) = 1, \quad U_\star(x, y, t = 0) = 1, \quad V(x, y, t = 0) = 0, \quad M(x, y, t = 0) = 0.2.$$

We take $\gamma = 1.4$, $Pr = 1$, and $\lambda(x, y, t = 0) = \gamma M^2/2$. The kinematic viscosity coefficient is $\nu = 3 \times 10^{-4}$. The Reynolds number based on the upstream flow states and the length L is $Re = \frac{LU_\star}{\nu} = 10^4$. No limiter is used in this case. The no-slip adiabatic boundary condition is imposed on the flat plate. Symmetry boundary condition is used for the other part of the bottom boundary. The non-reflecting boundary condition based on Riemann invariants is adopted at the left and the top boundaries. A first order extrapolation of cell average of the conservative variables is used at the right boundary. For details, see [38].

In Fig. 3.7, we show the P^1 solution of the velocity U in the x direction. The non-dimensional velocity U/U_\star at location $x = 0.5$ and $x = 1$ for both P^1 and P^2 cases are shown in Fig. 3.8, which are compared to the Blasius solution. In the plots, $\eta = y\sqrt{U_\star/(\nu x)}$, and we can see that the scheme with the P^2 solution space performs slightly better than that with the P^1 solution space.

4 Conclusion

In this paper, a novel CDG-BGK method for viscous flow simulations is proposed. The new scheme inherits several merits from both the CDG framework and the gas-kinetic BGK schemes. The fluxes in the BGK method is based on the particle transport and collisional mechanism via the gas-kinetic BGK model. Such fluxes take into account of both the convective and viscous terms, due to the intrinsic connection between the gas-kinetic BGK model and the Navier-Stokes equations. The CDG method evolves two pieces of approximate solutions defined on overlapping meshes. The cell interfaces of one computational mesh are inside the staggered mesh, hence the fluxes are in the continuous region of the staggered solution. For the CDG-BGK method, the distribution function in the interior of elements

is continuous and is much easier to evaluate than existing finite volume or DG BGK methods. Numerical results in 1D and 2D illustrate the accuracy and robustness of the proposed CDG-BGK scheme.

Acknowledgement. Research of the first author is partly supported by the scholarship from China Scholarship Council (CSC) under the Grant CSC No. 201206030032. The first, third and fourth authors are partially supported by Air Force Office of Scientific Computing YIP grant FA9550-12-0318, NSF grant DMS-1217008 and University of Houston. The authors would like to thank F.-Y. Li, H.-W. Liu and C.-W. Shu for helpful discussions about boundary conditions.

A Appendix

A.1 Physics notations

We describe physical parameters which are used in this paper. For the monatomic gas, the internal degree of freedom $N = 0$. For the diatomic gases, $N = 2$ accounts for two independent rotational degrees of freedom. Equipartition principle in statistical mechanics shows that each degree of freedom shares an equal amount of energy $\frac{1}{2}k_B T$, where k_B is Boltzmann constant. Then the heat capacity of C_p at constant pressure and C_v at constant volume for gases in equilibrium state have the forms

$$C_v = \frac{N + 3}{2}R; \quad C_p = \frac{(N + 3) + 2}{2}R,$$

where $R = k_B/m$ is the gas constant, the 3 accounts for the degree of freedom of molecular motion in x, y, z directions. From the above equations, we can obtain the ratio of specific heats,

$$\gamma = \frac{C_p}{C_v} = \frac{(N + 3) + 2}{N + 3}.$$

For a monatomic gas, $N = 0$, $\gamma = 5/3$. For a diatomic gas, $N = 2$, $\gamma = 7/5$. The Prandtl number is $Pr = \mu C_p / \kappa_q = 1$ for the BGK model. For a monatomic gas, the heat conduction coefficient becomes $\kappa_q = 5\mu R/2$.

A.2 1D and 2D moments

The evaluation of the Maxwellian is given in this section, the details can be found in [36]. For the 1D flow, the moments of Maxwellian g with respect to Q is introduced as,

$$\rho\langle Q \rangle = \int Q g d u d \xi,$$

and the general moment formula is

$$\langle u^n \xi^l \rangle = \langle u^n \rangle \langle \xi^l \rangle,$$

where n is integer, and l is an even integer. The moments of $\langle \xi^l \rangle$ are

$$\langle \xi^0 \rangle = 1, \quad \langle \xi^2 \rangle = \frac{K}{2\lambda}, \quad \langle \xi^4 \rangle = \frac{K(K+2)}{4\lambda^2}, \quad (\text{A.1})$$

and

$$\langle u^0 \rangle = 1, \quad \langle u^1 \rangle = U, \quad \langle u^{n+2} \rangle = U \langle u^{n+1} \rangle + \frac{n+1}{2\lambda} \langle u^n \rangle. \quad (\text{A.2})$$

For the 2D flow,

$$\rho\langle Q \rangle = \int Q g d u d v d \xi,$$

and the general moment formula is

$$\langle u^n v^m \xi^l \rangle = \langle u^n \rangle \langle v^m \rangle \langle \xi^l \rangle,$$

where n, m are integers, and l is an even integer. Here the moments $\langle u^n \rangle$ and $\langle \xi^l \rangle$ are the same as the 1D flow. The moments of v are

$$\langle v^0 \rangle = 1, \quad \langle v^1 \rangle = V, \quad \langle v^{n+2} \rangle = V \langle v^{n+1} \rangle + \frac{n+1}{2\lambda} \langle v^n \rangle. \quad (\text{A.3})$$

References

- [1] F. BASSI AND S. REBAY, *A high-order accurate discontinuous finite element method for the numerical solution of the compressible Navier–Stokes equations*, Journal of Computational Physics, 131 (1997), pp. 267–279.
- [2] P. L. BHATNAGAR, E. P. GROSS, AND M. KROOK, *A model for collision processes in gases. I. Small amplitude processes in charged and neutral one-component systems*, Physical Review, 94 (1954), pp. 511–525.

- [3] S. CHAPMAN AND T. G. COWLING, *The mathematical theory of non-uniform gases: an account of the kinetic theory of viscosity, thermal conduction and diffusion in gases*, Cambridge University Press, 1991.
- [4] S.-Y. CHOU AND D. BAGANOFF, *Kinetic flux–vector splitting for the Navier–Stokes equations*, Journal of Computational Physics, 130 (1997), pp. 217–230.
- [5] B. COCKBURN, G. E. KARNIADAKIS, AND C.-W. SHU, *The development of discontinuous Galerkin methods*, Springer, 2000.
- [6] B. COCKBURN, F. LI, AND C.-W. SHU, *Locally divergence-free discontinuous Galerkin methods for the Maxwell equations*, Journal of Computational Physics, 194 (2004), pp. 588–610.
- [7] B. COCKBURN, S.-Y. LIN, AND C.-W. SHU, *TVB Runge-Kutta local projection discontinuous Galerkin finite element method for conservation laws III: one-dimensional systems*, Journal of Computational Physics, 84 (1989), pp. 90–113.
- [8] B. COCKBURN AND C.-W. SHU, *Runge–Kutta discontinuous Galerkin methods for convection-dominated problems*, Journal of Scientific Computing, 16 (2001), pp. 173–261.
- [9] S. GODUNOV, *A finite difference scheme for numerical computation of the discontinuous wave solutions of equations of fluid dynamics*, Math. Sb., 47 (1959), pp. 271–306.
- [10] A. HARTEN, B. ENGQUIST, S. OSHER, AND S. R. CHAKRAVARTHY, *Uniformly high order accurate essentially non-oscillatory schemes, III*, Journal of Computational Physics, 71 (1987), pp. 231–303.
- [11] A. HARTEN, P. D. LAX, AND B. V. LEER, *On upstream differencing and Godunov-type schemes for hyperbolic conservation laws*, SIAM review, 25 (1983), pp. 35–61.
- [12] G.-S. JIANG AND C.-W. SHU, *Efficient Implementation of Weighted ENO Schemes*, Journal of Computational Physics, 126 (1996), pp. 202–228.

- [13] A. KURGANOV AND E. TADMOR, *New high-resolution central schemes for nonlinear conservation laws and convection–diffusion equations*, Journal of Computational Physics, 160 (2000), pp. 241–282.
- [14] J. LI, Q. LI, AND K. XU, *Comparison of the generalized Riemann solver and the gas-kinetic scheme for inviscid compressible flow simulations*, Journal of Computational Physics, 230 (2011), pp. 5080–5099.
- [15] Q. LI, S. FU, AND K. XU, *Application of gas-kinetic scheme with kinetic boundary conditions in hypersonic flow*, AIAA Journal, 43 (2005), pp. 2170–2176.
- [16] Q. LI, K. XU, AND S. FU, *A high-order gas-kinetic Navier–Stokes flow solver*, Journal of Computational Physics, 229 (2010), pp. 6715–6731.
- [17] W. LIAO, L.-S. LUO, AND K. XU, *Gas-kinetic scheme for continuum and near-continuum hypersonic flows*, Journal of Spacecraft and Rockets, 44 (2007), pp. 1232–1240.
- [18] H. LIU AND K. XU, *A Runge–Kutta discontinuous Galerkin method for viscous flow equations*, Journal of Computational Physics, 224 (2007), pp. 1223–1242.
- [19] X.-D. LIU, S. OSHER, AND T. CHAN, *Weighted essentially non-oscillatory schemes*, Journal of Computational Physics, 115 (1994), pp. 200–212.
- [20] Y. LIU, *Central schemes on overlapping cells*, Journal of Computational Physics, 209 (2005), pp. 82–104.
- [21] Y. LIU, C.-W. SHU, E. TADMOR, AND M. ZHANG, *Central discontinuous Galerkin methods on overlapping cells with a nonoscillatory hierarchical reconstruction*, SIAM Journal on Numerical Analysis, 45 (2007), pp. 2442–2467.
- [22] ———, *L_2 stability analysis of the central discontinuous Galerkin method and a comparison between the central and regular discontinuous Galerkin methods*, ESAIM: Mathematical Modelling and Numerical Analysis, 42 (2008), pp. 593–607.

- [23] —, *Central local discontinuous Galerkin methods on overlapping cells for diffusion equations*, ESAIM-Mathematical Modelling and Numerical Analysis, 45 (2011), pp. 1009–1032.
- [24] J. LUO, L. XUAN, AND K. XU, *Comparison of Fifth-Order WENO Scheme and Finite Volume WENO-Gas-Kinetic Scheme for Inviscid and Viscous Flow Simulation*, Communications in Computational Physics, 14 (2013), pp. 599–620.
- [25] J. MANDAL AND S. DESHPANDE, *Kinetic flux vector splitting for Euler equations*, Computers & Fluids, 23 (1994), pp. 447–478.
- [26] G. MAY, B. SRINIVASAN, AND A. JAMESON, *An improved gas-kinetic BGK finite-volume method for three-dimensional transonic flow*, Journal of Computational Physics, 220 (2007), pp. 856–878.
- [27] H. NESSYAHU AND E. TADMOR, *Non-oscillatory central differencing for hyperbolic conservation laws*, Journal of Computational Physics, 87 (1990), pp. 408–463.
- [28] G. NI, S. JIANG, AND K. XU, *A DGBGK scheme based on WENO limiters for viscous and inviscid flows*, Journal of Computational Physics, 227 (2008), pp. 5799–5815.
- [29] S. OSHER AND F. SOLOMON, *Upwind difference schemes for hyperbolic systems of conservation laws*, Mathematics of computation, 38 (1982), pp. 339–374.
- [30] P. L. ROE, *Approximate Riemann solvers, parameter vectors, and difference schemes*, Journal of Computational Physics, 43 (1981), pp. 357–372.
- [31] C.-W. SHU, *Total-variation-diminishing time discretizations*, SIAM Journal on Scientific and Statistical Computing, 9 (1988), pp. 1073–1084.
- [32] C.-W. SHU AND S. OSHER, *Efficient implementation of essentially non-oscillatory shock-capturing schemes*, Journal of Computational Physics, 77 (1988), pp. 439–471.
- [33] E. F. TORO, *Riemann solvers and numerical methods for fluid dynamics: a practical introduction*, Springer, 2009.

- [34] B. VAN LEER, *Towards the ultimate conservative difference scheme. V. A second-order sequel to Godunov's method*, Journal of Computational Physics, 32 (1979), pp. 101–136.
- [35] K. XU, *Gas-kinetic schemes for unsteady compressible flow simulations*, Lecture series-van Karemman Institute for fluid dynamics, 3 (1998), pp. C1–C202.
- [36] —, *A gas-kinetic BGK scheme for the Navier–Stokes equations and its connection with artificial dissipation and Godunov method*, Journal of Computational Physics, 171 (2001), pp. 289–335.
- [37] —, *Discontinuous Galerkin BGK method for viscous flow equations: one-dimensional systems*, SIAM Journal on Scientific Computing, 25 (2004), pp. 1941–1963.
- [38] K. XU AND Z. LI, *Dissipative mechanism in Godunov-type schemes*, International Journal for Numerical Methods in Fluids, 37 (2001), pp. 1–22.
- [39] K. XU, M. MAO, AND L. TANG, *A multidimensional gas-kinetic BGK scheme for hypersonic viscous flow*, Journal of Computational Physics, 203 (2005), pp. 405–421.
- [40] K. XU AND K. H. PRENDERGAST, *Numerical Navier-Stokes solutions from gas kinetic theory*, Journal of Computational Physics, 114 (1994), pp. 9–17.

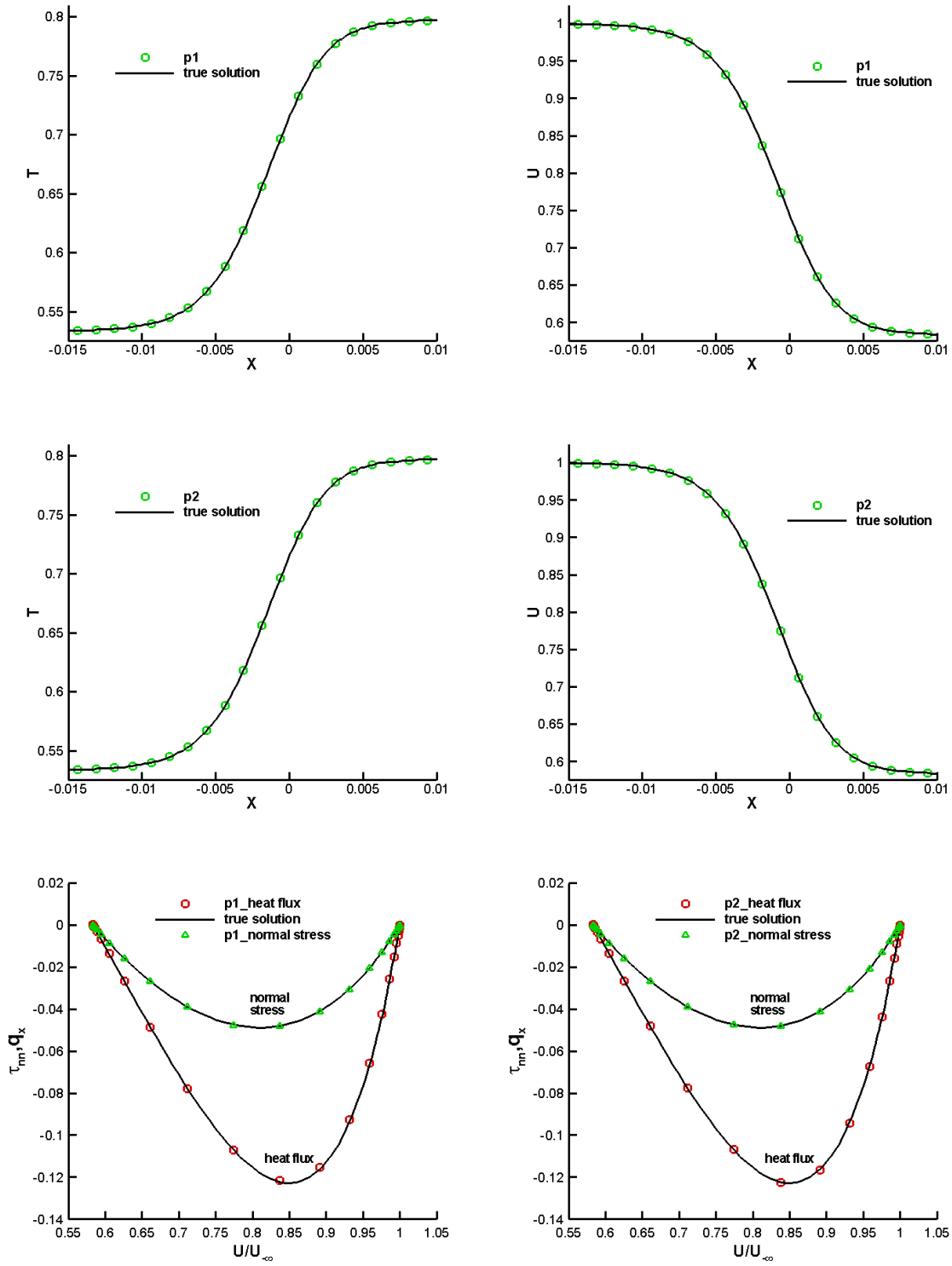


Figure 3.3: Navier-Stokes shock structure calculation, P^1 and P^2 case.

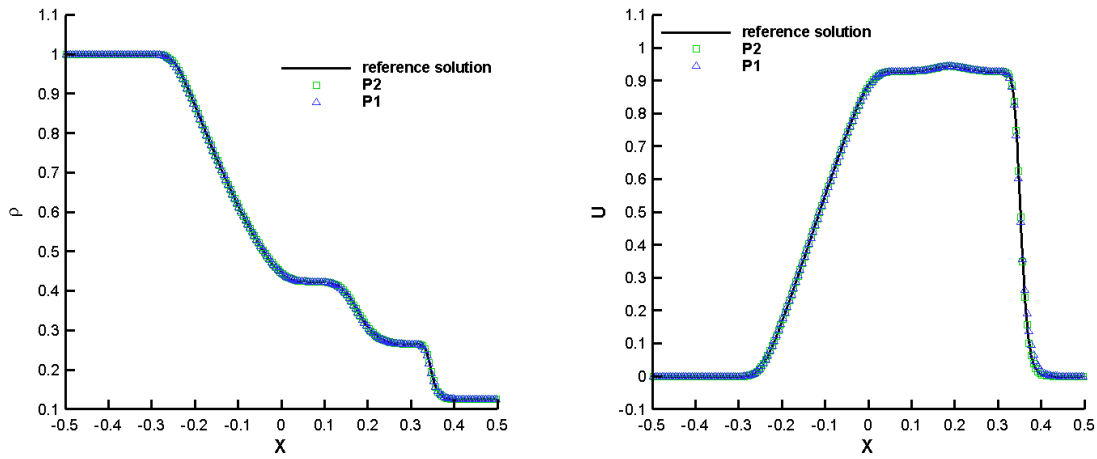


Figure 3.4: Shock tube problem for the Navier-Stokes equations with kinematic viscosity coefficient $\nu = 0.0005/\rho\sqrt{\lambda}$.

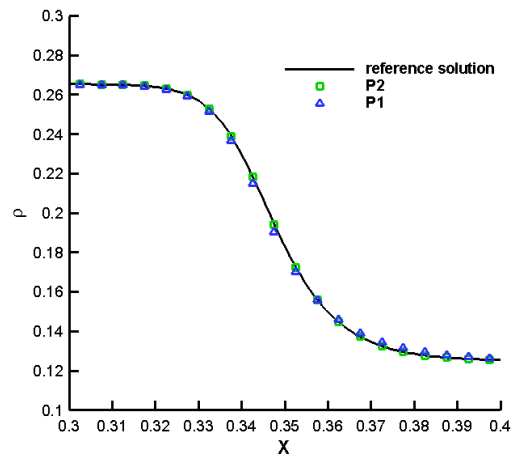


Figure 3.5: The zoom-in view of the density distribution around the shock wave in shock tube test with $\nu = 0.0005/\rho\sqrt{\lambda}$.

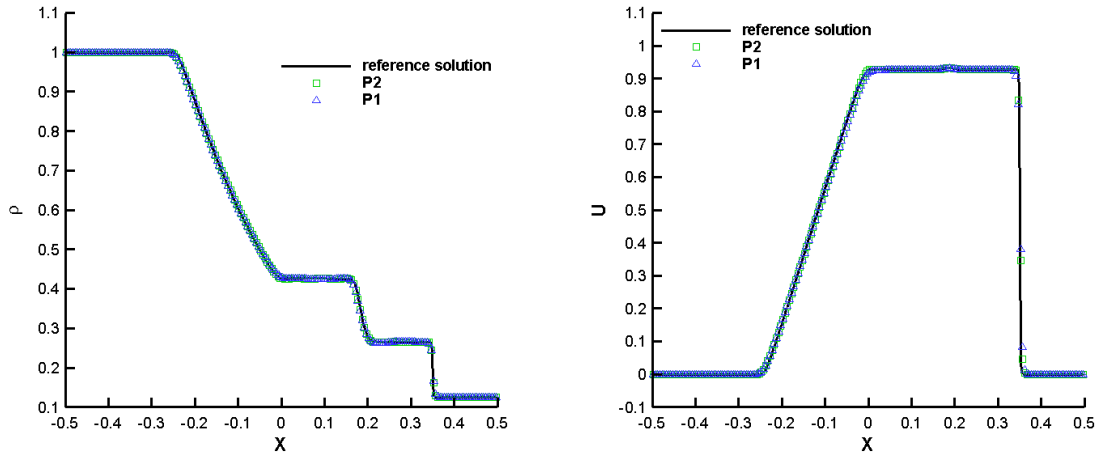


Figure 3.6: Shock tube problem for the Navier-Stokes equations with kinematic viscosity coefficient $\nu = 0.00005/\rho\sqrt{\lambda}$.

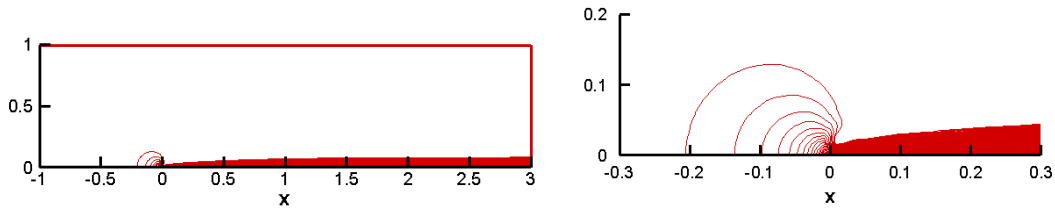


Figure 3.7: Laminar boundary layer, contour of velocity obtained by P^1 case. The right plot is the zoom-in plot of the interesting region in the left plot.

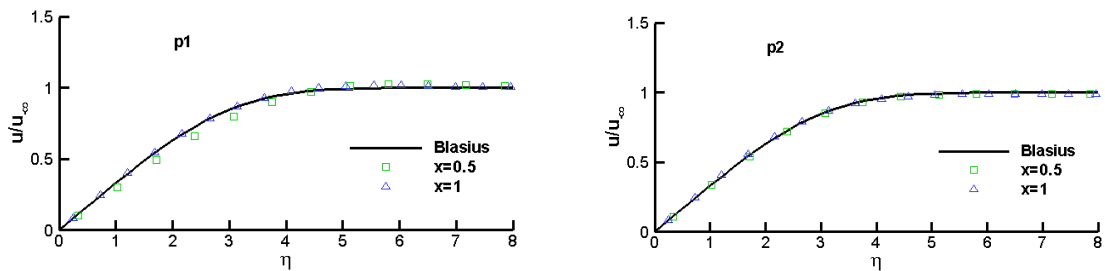


Figure 3.8: Laminar boundary layer, U velocity distribution along two vertical lines benchmarked with the Blasius solution. CDG solutions with P^1 and P^2 solution spaces.